photonics

MDPI

Article

New Insights Reached via Graded-Interfaces Modeling: How High-Power, High-Efficiency Mid-Infrared QCLs Work

Dan Botez [1,*], Suraj Suri [1], Huilong Gao [1], Thomas Grange [2], Jeremy D. Kirch [1], Luke J. Mawst [1] and Robert A. Marsland [3]

[1] Department of Electrical and Computer Engineering, University of Wisconsin-Madison, Madison, WI 53706, USA; suri5@wisc.edu (S.S.); hgao48@wisc.edu (H.G.); jdkirch@wisc.edu (J.D.K.); ljmawst@wisc.edu (L.J.M.)
[2] Nextnano Lab, 12 Chemin des Prunelles, 38700 Corenc, France; thomas.grange@nextnano.com
[3] Intraband, LLC, Madison, WI 53726, USA; robm@intraband.us
* Correspondence: botez@engr.wisc.edu

Abstract: Graded-interfaces modeling unveils key features of high-power, high-efficiency quantum-cascade lasers (QCLs): direct resonant-tunneling injection from a prior-stage, low-energy state into the upper-laser (*ul*) level, over a wide (~50 nm) multiple-barrier region; and a new type of photon-induced carrier transport (PICT). Stage-level QCL operation primarily involves two steps: injection into the *ul* level and photon-assisted diagonal transition. Furthermore, under certain conditions, a prior-stage low-energy state, extending deep into the next stage, *is* the *ul* level, thus making such devices *injectionless* QCLs and leading to stronger PICT action due to quicker gain recovery. Thermalization within a miniband ensures population inversion between a state therein and a state in the next miniband. Using graded-interfaces modeling, step-tapered active-region (STA) QCLs possessing PICT action have been designed for carrier-leakage suppression. A preliminary 4.6 μm emitting STA design of a metal–organic chemical-vapor deposition (MOCVD)-grown QCL led to an experimental 19.1% front-facet, peak wall-plug efficiency (WPE). Pure, diffraction-limited beam operation is obtained at 1.3 W CW power. A low-leakage 4.7 μm emitting design provides a projected 24.5% WPE value, considering MOCVD-growth, graded-interface interface-roughness (IFR) parameters, and waveguide loss (α_w). The normalized leakage-current density, J_{leak}/J_{th}, is 17.5% vs. 28% for the record-WPE 4.9 μm emitting QCL. Then, when considering the IFR parameters and α_w values of optimized-crystal-growth QCLs, J_{leak}/J_{th} decreases to 13.5%, and the front-facet WPE value reaches 33%, thus approaching the ~41% fundamental limit. The potential of graded-interfaces modeling to become the design tool for achieving room-temperature operation of terahertz QCLs is discussed.

Keywords: graded-interfaces modeling; prior-stage injection into upper laser level; injectionless quantum cascade laser; photon-induced carrier transport; interface-roughness scattering; thermally activated shunt-type carrier leakage; high wall-plug efficiency; terahertz quantum cascade laser

Received: 2 December 2024
Revised: 16 January 2025
Accepted: 17 January 2025
Published: 21 January 2025

Citation: Botez, D.; Suri, S.; Gao, H.; Grange, T.; Kirch, J.D.; Mawst, L.J.; Marsland, R.A. New Insights Reached via Graded-Interfaces Modeling: How High-Power, High-Efficiency Mid-Infrared QCLs Work. *Photonics* **2025**, *12*, 93. https://doi.org/10.3390/photonics12020093

1. Introduction

Recently, by employing a non-equilibrium Green's functions (NEGF), graded-interfaces model modified for the multiband case of mid-infrared (IR)-emitting QCLs [1], we were able to reproduce, for the first time, the electro-optical characteristics of record-performance 4.9 μm and 8.3 μm emitting QCLs [2,3]. The interface-roughness (IFR)

parameters at various interfaces were deduced from measured values and trends found via atom-probe tomography (APT) analysis of a 4.6 μm emitting QCL structure of varying active-region barrier heights [4]. The employed IFR parameters' values were further validated by sensitivity analyses of the devices' performances to variations in graded-interface IFR-parameters values [1]. We found that, despite the record-high, front-facet wall-plug efficiency (WPE) values [2,3] (i.e., 27% and 17%, respectively), there is a significant normalized leakage-current density, J_{leak}/J_{th}, of ~28% and ~23%, primarily because of IFR-triggered, shunt-type leakage through high-energy active-region states [5,6]. Then, the graded-interfaces model, besides allowing us to understand how high-power mid-IR QCLs work, becomes a design tool for mid-IR QCLs of even higher performances by suppressing carrier leakage via the step-taper active-region (STA) design [7]. For instance, we designed [1] an 8.1 μm emitting STA QCL of substantially suppressed carrier leakage, which provided a front-facet wall-plug efficiency value of 22.2%; thus, a value close to the 25% upper limit for ~8 μm emitting QCLs [6]. Notably, analyses of high-resolution X-ray-diffraction spectra of QCL structures grown by metal–organic chemical-vapor deposition (MOCVD) [8–10] have indicated no significant changes in layer thicknesses and/or compositions across the entire QCL core region. Therefore, graded-interfaces modeling is a valid design tool for both molecular-beam epitaxy (MBE)- and MOCVD-grown QCL structures.

It should be pointed out that APT analysis of the MOCVD-grown AlInAs/GaInAs interfaces of specific 8–9 μm emitting QCL structures [8,11] did reveal that the interfaces were asymmetrically graded and that there was excess indium (In) at the AlInAs-to-GaInAs interfaces. Both features were primarily attributed to In segregation, while the grading was also partially attributed to hydrodynamic dispersion in the reactor. The authors did not use those APT-found interface gradings for device design. Instead, by using in-house historically measured QCL electroluminescence wavelengths, a symmetric graded-interface full-width value was empirically determined [11], using the error-function definition [12], which was successfully employed to explain the relatively large (0.5–1.0 μm) lasing-wavelength redshifts for lattice-matched QCLs between abrupt-interface designs and experiment [8,11]. Those lasing-wavelength redshifts are somewhat like the relatively small (0.2 μm) redshift we found [1] between abrupt- and graded-interfaces, strain-compensated 8.3 μm emitting QCL designs. In addition, by considering the deduced empirical graded-interface width for device design, high-performance 7.5 μm, 8 μm, and 8.5 μm emitting QCLs were achieved [8,11,13]. However, the graded-interface IFR-scattering parameters could not be extracted via APT. Thus, one could not employ graded-interface IFR scattering for designing QCLs of even higher performances.

Here, we describe the injection mechanism into the upper-laser (*ul*) level at work in record-high performance mid-IR QCLs operating at room temperature. That is, we discuss sequential resonant-tunneling injection from prior-stage, low-energy states into the *ul* level, over wide (~50 nm) multiple-barrier regions, for two different cases: (a) from threshold, and (b) from the resonance point with the first injecting state. For the latter, the prior-stage energy state *is* the *ul* level from threshold up to its resonance with the next-higher-energy state; thus, over that drive-level range, the device is an *injectionless* QCL. Both behaviors strengthen the photon-induced carrier transport (PICT) action in high-power mid-IR QCLs, which we show to be quite different compared to the PICT action previously modeled [14,15] for low-power, mid-IR QCLs operating at cryogenic temperatures.

Then, we present STA-QCL designs, possessing PICT action, for devices emitting at 4.6–4.7 μm wavelength, and the results such obtained. By using a preliminary design that employs the graded-interface IFR parameters measured via APT of MOCVD-grown

STA-QCL structures [4], we experimentally obtain a front-facet, maximum WPE value of 19.1%, which is the highest such value reported to date for MOCVD-grown QCLs as well as the second-highest front-facet WPE value reported to date for any QCL operating at room temperature. Excellent agreement is obtained between theoretically predicted and experimentally obtained electro-optical characteristics, thus validating our model. Further design optimization, for substantially reducing the J_{leak}/J_{th} value, results in a MOCVD-growth 4.7 μm emitting device of projected 24.5% maximum front-facet WPE value. Subsequently, by considering the graded-interface IFR-parameter values [1] and the low waveguide-loss value [2] obtained from 4.9 μm emitting QCLs grown by optimized gas-source molecular-beam epitaxy (GSMBE) [2], the low-leakage, 4.7 μm emitting STA-QCL design provides a maximum front-facet WPE value of 33%; that is, a value higher than the current record front-facet value (i.e., 27 %) and approaching the fundamental upper limit of ~ 41% for ~4.7 μm emitting QCLs [6].

Finally, in the Section 5, we briefly discuss the potential of graded-interfaces modeling as the design tool for achieving terahertz (THz) QCL operation at room temperature.

2. Injection Mechanism

Zoomed-in portions of the conduction-band diagram and wavefunctions relevant as far as which energy state is the *ul* level, at threshold, are shown in Figure 1a,b for the record-performance 8.3 μm emitting QCL [3] and for a 4.7 μm emitting STA-type QCL (discussed below in Section 4.2.2), respectively, modeled with graded interfaces and possessing PICT action. For the 8.3 μm emitting device the prior-stage, low-energy states 2 and 2′, located just below the lower-laser (*ll*) level, state 3, are the same as the stage-of-interest energy states g_3 and 4, respectively (see Figure 1a), as confirmed by the fact they have identical sheet-carrier density and electron temperature (e.g., the electron temperature at threshold, $T_{e,th}$, in the 2′/4 state is 445 K). State 4 was found [1] to be the *ul* level. The reason why state 4 is the *ul* level, rather than state g_3, is because the differential gain (in the absence of carrier leakage) [6] is 1.3 times higher for the 4-*ll* transition than for the g_3-*ll* transition. More specifically, the key part of the differential-gain expression is the so-called figure of merit, $\tau_{up,g,n}\ z_{n,ll}^2$, where $\tau_{up,g,n}$ is the global 'effective' lifetime [7] characterizing all transitions between a high-energy active-region (AR) energy state *n*, and all low-energy AR states, and $z_{n,ll}$ is dipole-matrix element characterizing the transition between state *n* and the *ll* level. For the 8.3 μm-emitting QCL the figure of merit is 1.2 times higher for state 4 than for state g_3. Thus, the 4-*ll* transition is the one favored to lase.

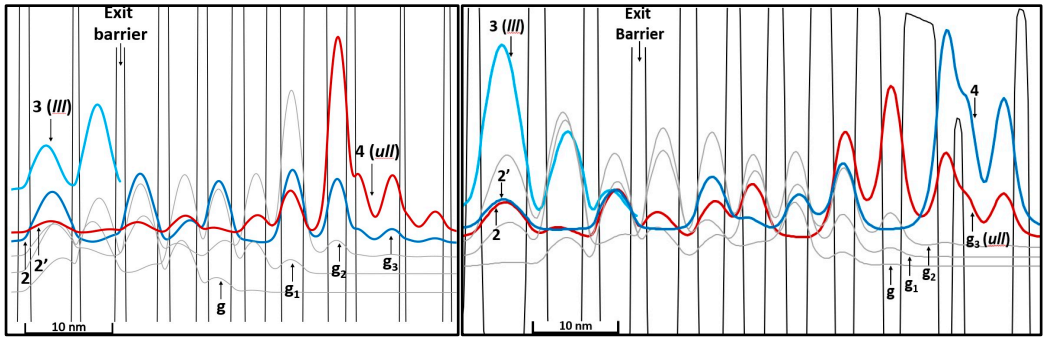

(**a**) (**b**)

Figure 1. Zoomed-in conduction-band diagram and relevant wavefunctions, at threshold: (**a**) 8.3 μm emitting QCL [3], for which injection occurs from a prior-stage energy state, state 2, into the *ul* level, state 4; and (**b**) 4.7 μm emitting STA-QCL design (see Section 4.2.2), for which state 2/g_3 both injects into state 4 and it is the *ul* level (see text for details).

The *ul*-level wavefunction extends deep to the left and slightly penetrates the prior stage, while the state $2/g_3$ wavefunction penetrates deep (~50 nm) into the stage of interest. We conclude that states 4 and 2 are delocalized due to resonant tunneling through ~8 barriers, and that there is resonant-tunneling injection, in the presence of scattering [16], from state 2 into the *ul* level, over an ~50 nm wide region. That is, the indicated "exit" barrier is not the extraction/injection barrier into a next-stage state, since extraction/injection occurs over ~8 barriers. For the 8.3 μm emitting device resonant-tunneling injection, at threshold, happens when, at a field F_{th} = 43.2 kV/cm, levels 2 and 4 are 8.9 meV apart, while resonance occurs at 1.76 × threshold, at a field of 45.5 kV/cm, where the energy splitting is 6.6 meV. That is, to start with, the QCL has moderately strong coupling. The first analyses of PICT action in QCLs [14,15] had the injector ground state being identical with the *ul* level; that is, the injecting state and the *ul* level were degenerate. Besides injection and lasing transition, in those cases, carrier transport also involved two other steps: tunneling from the *ll* level of the prior stage into an injector-miniband state, followed by electron scattering down to the injector ground state/*ul* level. By contrast, in high-performance mid-IR QCLs with PICT action, for which at threshold the injected-in state is the *ul* level, there is only injection into the *ul* level, from a prior-stage low-energy state, followed by the lasing transition and thermalization from the *ll* level to the next injecting state.

For the 4.7 μm emitting STA QCL (Figure 1b), the injection scheme is the same: resonant-tunneling injection from a prior-stage low-energy state, state 2, into state 4 over an ~50 nm wide region. However, the differential-gain value for the $2/g_3$-*ll* transition is found to be twice that for the 4-*ll* transition. (in this case the figure of merit for state g_3 is 1.85 times higher than that for state 4, since the g_3-*ll* transition is strongly diagonal (i.e., $\tau_{up,g,g3}$ is 4.27 ps and $z_{g3,ll}$ is 0.62 nm)). Then, state $2/g_3$ is the *ul* level at threshold and continues to be the *ul* level up to and at the $2/g_3$-4 resonance, at 1.8 × threshold. Beyond 1.8 × threshold state 4 becomes the *ul* level and remains so up to laser shutoff. Similar behavior was observed [1] for the 4.9 μm emitting record-WPE QCL [2]; in that, state g_4 was found to be the *ul* level up to and at the resonance with state 4, at 1.4 × threshold, beyond which state 4 was found to be the *ul* level.

Direct resonant-tunneling injection into the *ul* level, at threshold or at some point above threshold, is fundamentally different than injection into the *ul* level in conventional mid-IR QCLs. That is, for the latter, after electrons are extracted through the prior-stage exit barrier, they cool down via scattering to the injector ground state, *g*, and lasing starts at a higher field when, upon resonant-tunneling injection from state *g* into the *ul* level [17], the states align to reach the necessary detuning for lasing action [17,18]. Furthermore, in the case of direct injection into the *ul* level at threshold, the injecting state and the *ul* level reach resonance relatively close above threshold [1], unlike in conventional QCLs for which the *g*-*ul* resonance is reached high above threshold at the maximum current density, J_{max}. By contrast, for direct injection, after the 2-*ul* resonance point, there is sequential injection into the *ul* level, with J_{max} typically occurring at the g_1-*ul* resonance. For example, for the 8.3 μm emitting QCL after the $2/g_3$-4 resonance at the 1.76 × threshold, there is resonant-tunneling injection over ~8 barriers from state g_2 into state 4, up to their resonance at 3.75 × threshold (Figure 2a), followed by resonant-tunneling injection over ~8 barriers from state g_1 into state 4, up to their resonance at J_{max} (Figure 2b).

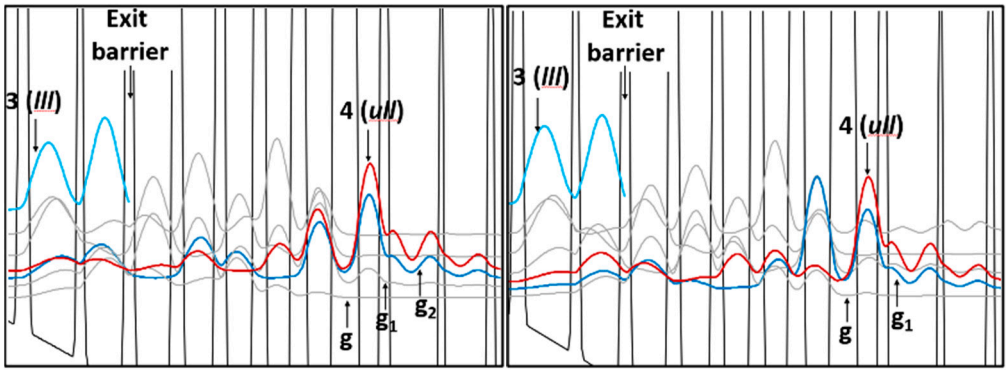

(**a**) (**b**)

Figure 2. Zoomed-in conduction-band diagram and relevant wavefunctions for 8.3 μm emitting QCL [3]: (**a**) at the resonance point between the injecting state g_2 and the *ul* level, at 3.75 × threshold (7 meV splitting); and (**b**) at the resonance point between the injecting state g_1 and the *ul* level, at 4 × threshold (7.5 meV splitting) where the device shuts off (i.e., J_{max} is reached).

3. Photon-Induced Carrier Transport in High-Performance Mid-IR QCLs

We analyze the 8.3 μm emitting QCL, since out of all devices studied in Ref. [1], it has the simplest lasing transition at threshold, that is, primarily from the *ul* level to one *ll* level, level 3. The entire band diagram for the 8.3 μm emitting QCL is shown in Figure 3. As pointed out above, injection occurs into the *ul* level, state 4, from the prior-stage low-energy state, state 2. The lasing transition occurs between states 4 and 3. That corresponds to a strong diagonal transition of a relatively low matrix-element value, z_{43} = 13.7 Å. The corresponding lifetime, τ_{43}, has a value of 2.56 ps, while the global *ul*-level lifetime, $\tau_{ul,g}$, is 0.99 ps. The *ll* level is depopulated both by extraction to state 3′ as well as by relaxation, via LO-phonon and IFR scattering, to levels 2, 2′, 2″, 1′ and 1, which provides a low global *ll*-level lifetime $\tau_{ll,g}$ of 0.12 ps. Assuming an extraction lifetime [15] of ~0.5 ps, the effective *ll*-level lifetime is ~0.10 ps. Thus, we have the main ingredients for strong PICT action: (a) fast depopulation of the *ll* level, followed by strong-coupling injection into the next-stage *ul* level, which together ensure quick gain recovery; and (b) strong diagonal transition, which ensures photon-assisted tunneling [14,15]. The latter reduces the transit time. As a result of PICT action, the differential resistance, R_{diff}, value is 60% that for a conventional QCL of same pumping area [1], and the J_{max} value is 17% higher than that for a conventional QCL of same sheet-doping density [1].

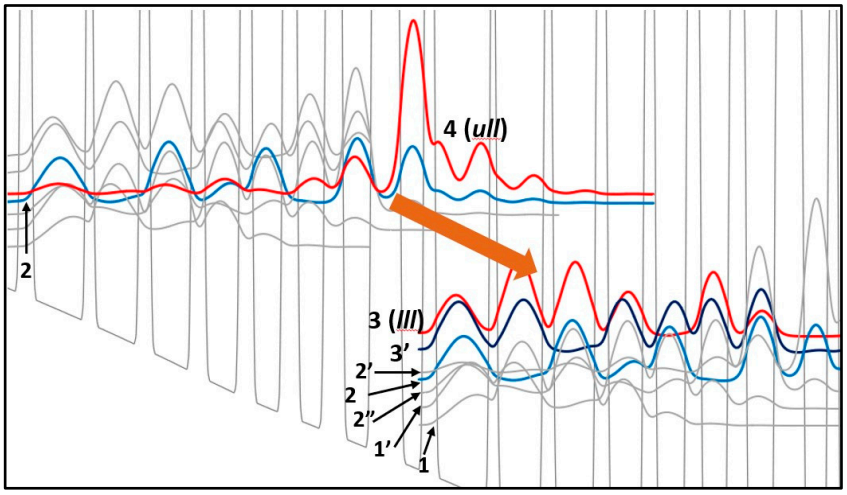

Figure 3. Schematic representation of photon-induced carrier transport for the 8.3 μm emitting QCL [3]. The orange arrow indicates a strong diagonal lasing transition.

This PICT action is quite different compared to those found for previously studied mid-IR QCLs [15,19,20]. The first in-depth study [15] was of devices operating at 30 K, which had the following features: the *ll*-level depopulation was ensured via extraction to the next stage; carrier transport occurred through a superlattice region down to the injector ground state, which was also the *ul* level (in effect strong coupling occurred); and a strong diagonal transition. The second study [19] involved a device operating at room temperature [21,22], which, for frequency-tuning purposes, had on purpose weak coupling between the injecting state and the *ul* level, ensuring a moderately high R_{diff} value [6], as required for efficient tuning of the lasing wavelength by varying the drive current. However, the device had a diagonal lasing transition in the active-region portion beyond the injection barrier, which ensured photon-assisted tunneling [19,21]. Thus, for that device PICT action involved only the photon-assisted tunneling associated with the lasing transition. Similarly, for a device designed for high-WPE operation at cryogenic temperatures (40–80 K) [23], for which there was weak coupling to the *ul* level and a diagonal transition beyond the injection barrier, PICT action was identified [20] at 40 K, as a decrease in the R_{diff} value when lasing action was considered.

A schematic representation of PICT action in high-performance mid-IR QCLs, for which the injected-in state at threshold is the *ul* level, is shown in Figure 4. After injection from a prior-stage energy state into the *ul* level, a strong diagonal transition occurs from the *ul* level to the *ll* level. The *ll* level is depopulated to all energy states below it, as well, by extraction to the next stage. An energy state situated below the *ll* level is the state injecting into the *ul* level of the next stage. Thus, unlike in Ref. [15], in this case, gain recovery is primarily limited only by the injection time into the *ul* level. Of course, for QCLs for which, at threshold, the injecting state is also the *ul* level (Figure 1b), the schematic representation in Figure 4 applies only above the resonance point between the injecting state and the injected-in state. However, PICT action occurs from threshold, like for the initial PICT-action QCL [14,15], for which the injector ground state was also the *ul* level.

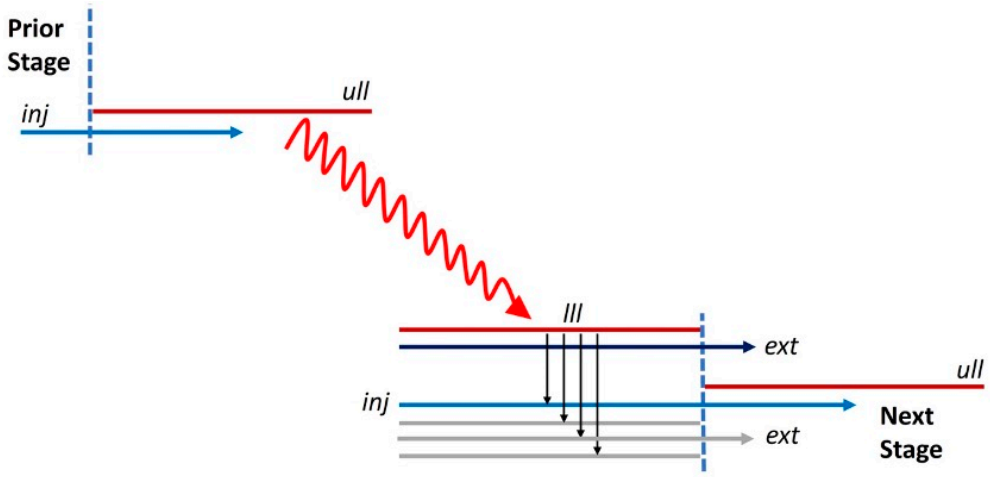

Figure 4. Schematic representation of PICT action in high-power, high-efficiency mid-IR QCLs when there is injection at threshold into the *ul* level. The red wavy arrow indicates the lasing transition.

Furthermore, when the injecting state is also the *ul* level, the *only* time delay for gain recovery is the depopulation time of the *ll* level, that is, a very short time ($\leq$0.1 ps), ensuring, as we shall see, even stronger PICT action. In addition, the QCL stage-level operation becomes even simpler than that sketched in Figure 4: a lasing transition, followed by *ll*-level thermalization to the next-stage *ul* level; that is, the device is an injectionless QCL.

These are simple pictures, but they raise the question of how the injecting state and/or the *ul* level are/is populated. For that purpose, we plot first, at threshold (i.e., at

43.2 kV/cm), the wavefunctions for the prior-stage low-energy states and the high-energy states in the stage of interest (Figure 5a). These wavefunctions form a "de facto" miniband, since there are strong resonant extractions [1] between states 3 and 3′ (16.7 meV splitting energy at 43 kV/cm), states 2 and 2′ (6.6 meV splitting energy at 45.3 kV/cm), and states 2 and 2″ (12.4 meV splitting energy at 39.7 kV/cm). Thus, the carrier transport is basically like that in the miniband of bound-to-continuum QCLs [24].

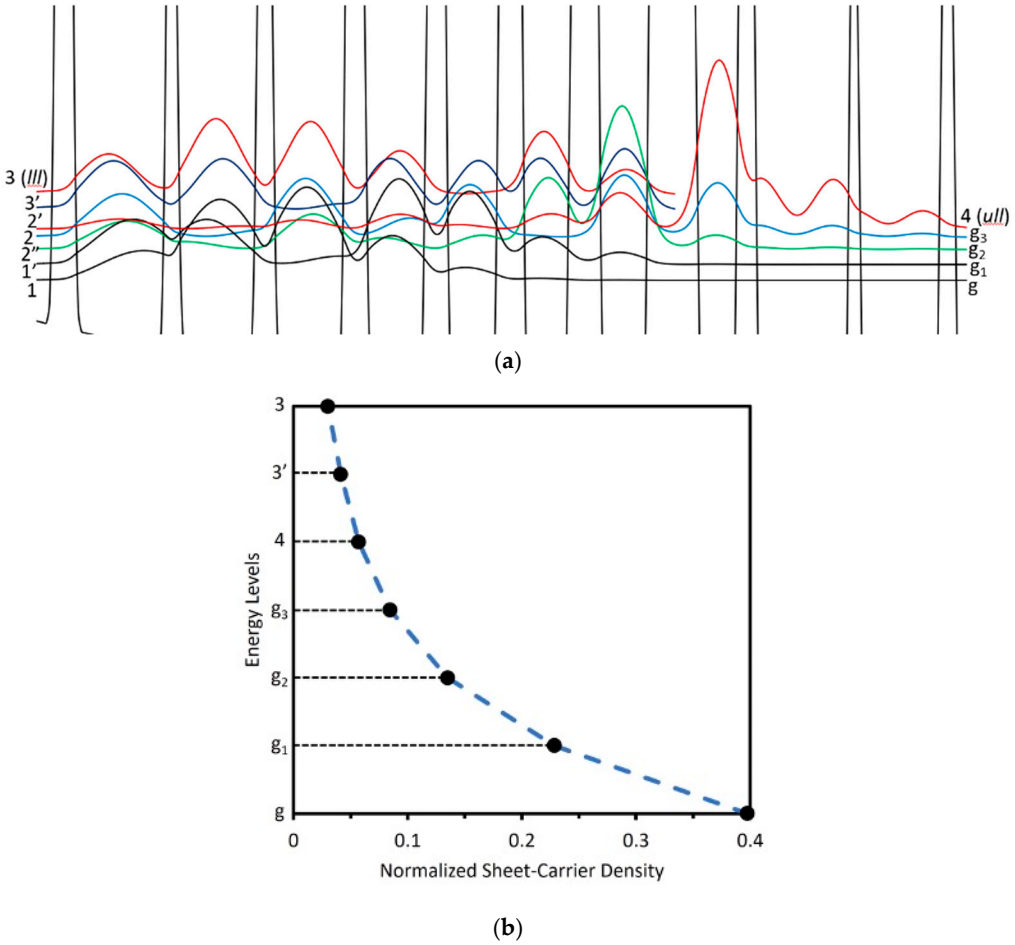

Figure 5. The 8.3 μm emitting QCL [3] at threshold (43.2 kV/cm): (**a**) wavefunctions for the low-energy states in the prior stage and the high-energy states in the stage of interest; and (**b**) normalized sheet-carrier densities in the miniband.

Then, in Figure 5b, we show the normalized sheet-carrier density for each energy state, at threshold, as obtained from NEGF modeling. The sheet-carrier distributions reflect thermal excitation via LO-phonon and IFR scattering from the ground state, g, to higher energy states as well as the subsequent thermalization. The thermalization is faster than the extraction from within the miniband (which is mainly controlled by the injection time into the *ul* level and the leakage through high-energy states [1] from the *ul* level and state g_3), as evidenced by the fact that the energy-states occupation factor decreases with increasing energy. Thus, there is no population inversion between the miniband states. However, since the population of the *ul* level (state 4), n_{ul}, is higher than the population of the *ll* level (state 3), n_{ll}, there is population inversion between state 4 of the shown miniband and state 3 of the next miniband in the stage of interest (see Figure 3). For example, for the 8.3 μm emitting QCL the n_{ul} and n_{ll} values are found to be 6.2×10^9 cm^{-2} and 3.2×10^9 cm^{-2}, respectively. That is, the population inversion needed for lasing is automatically set up, at threshold, by the distribution of sheet-carrier densities within a given miniband. For

devices for which state g_3 is the *ul* level at threshold, the population inversion occurs between state g_3 of the miniband, and state 3 of the next miniband.

Note that, previously, we used [1] the sheet-carrier densities in states g through 4, as well as their respective electron temperatures, for calculating the shunt-type carrier-leakage currents through the high-energy states 5 and 6. The sheet-carrier densities in states 3 and 3′ are not relevant as far as carrier leakage, since their wavefunctions have negligible overlap at well/barrier interfaces with the state-5 and -6 wavefunctions.

4. STA-Type 4.6–4.7 μm Emitting QCLs with PICT Action

The analysis [1] of record-WPE mid-IR QCLs [2,3] has uncovered that they both have PICT action, as well as relatively high normalized leakage-current density, $J_{\text{leak}}/J_{\text{th}}$, values: 23–28%. Therefore, we proceed to use the graded-interfaces NEGF model in conjunction with conduction-band engineering for suppressing carrier leakage in order to raise the WPE values of 4.6–4.7 μm emitting QCLs close to fundamental upper limits [6].

Since carrier leakage is dominated by IFR-triggered leakage [1,5], we show, as an example, the expression for the IFR leakage-current density [5] from the *ul* level through the high-energy state 5:

$$J_{leak,ul,5}^{IFR} = \frac{en_{ul}}{\tau_{5,ul}^{IFR}} \frac{\tau_{5,tot}^{LO,IFR,AD}}{\tau_{5,leak}^{LO,IFR,AD}} I_{nm}\left(\frac{E_{5,ul}}{kT_{e,ul}}\right) \exp\left(-\frac{E_{5,ul}}{kT_{e,ul}}\right) \quad (1)$$

where the *IFR* backscattering rate from state 5 to the *ul* level is given by the following [1]:

$$\frac{1}{\tau_{5,ul}^{IFR}} \cong \frac{\pi}{\hbar^3}\Lambda^2 F m_{c,ul} exp\left(-\frac{\Lambda^2 m_{c,ul} E_{5,ul}}{2h^2}\right) \sum_i \Delta_i^2 \delta V_i^2 \varphi_5^2(z_i)\varphi_{ul}^2(z_i) \quad (2)$$

where $m_{c,ul}$ is the effective mass in the *ul* level, δV_i is the conduction-band offset at the ith interface, and $\varphi_5(z_i)$ and $\varphi_{ul}(z_i)$ are the state-5 and *ul*-level wavefunction amplitudes at the ith interface. $E_{5,ul}$ represents the energy difference between states, and Λ is taken to be the same at all interfaces, as found to be primarily correct from APT analysis [4]. F is scattering-rate reduction factor due to graded interfaces. Note that, unlike in Ref. [1], for more accurate calculations [1], we consider the energy-dependent effective mass of the transition's final state.

From Equations (1) and (2), it is clear that in order to suppress leakage: (a) the $E_{5,ul}$ value should be maximized; and (b) the sum of probability products at interfaces between the *ul* level and high-energy state 5 (i.e., $\sum_i \varphi_5^2(z_i)\varphi_{ul}^2(z_i)$), a quantify we call [5] Interface Overlap Factor (IOF), should be minimized.

The STA design approach [7], that is, barrier heights and well depths increasing stepwise (downstream) in the optical-transition region, satisfies both conditions for carrier-leakage suppression (i.e., high $E_{5,ul}$ values [7] and low IOF values [5]). Therefore, we proceeded to design 4.6–4.7 μm emitting STA-type QCL with PICT action.

4.1. Preliminary-Design 4.6 μm Emitting STA-QCL with PICT Action

The design was performed by taking into account the IFR parameters found via APT for our MOCVD-grown 4.6 μm emitting STA-QCL structures [4]: Δ values of 0.14 nm at moderate-strain $Al_{0.65}In_{0.35}As$ barriers' interfaces, and 0.2 nm at highly strained (i.e., 1.3 nm thick AlAs) barrier interfaces, Λ = 6 nm and L = 0.55 nm, where Δ is the root-mean square height; Λ is the in-plane correlation length, and L is the graded-interface width. A value of 0.1 nm was chosen [1] for the axial correlation length, $\Lambda_\perp$. In addition, the trend in Δ values found in Ref. [4]; that is, the Δ value increases with increased strain in the AlInAs barriers, was considered.

The conduction-band diagram and relevant wavefunctions are shown in Figure 6. The device is an STA-type QCL since, in the optical-transition region, there are two moderate-height barriers ($Al_{0.60}In_{0.40}As$ and $Al_{0.65}In_{0.35}As$) followed by a tall, 1.2 nm thick barrier (AlAs). As a result, at threshold, the relevant energy difference, E_{54}, is 132 meV, a value higher than that for the linear-tapered 4.9 μm emitting record-WPE QCL [2] at threshold [1]: 114 meV. In this case, state 4 is the *ul* level at threshold. The splitting energy at the g_3-4 resonance (76 kV/cm) is 8.8 meV; thus, there is strong coupling. In addition, the device has a strong diagonal lasing transition (i.e., $z_{ul,ll}$ = 8 Å). However, the energy state g_4 is a parasitic one, which, as we shall see below, causes significant additional carrier leakage.

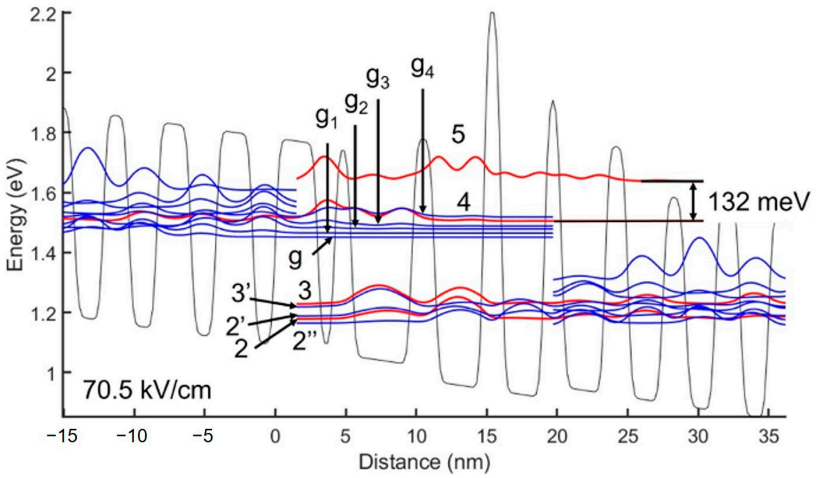

Figure 6. Conduction−band diagram and relevant wavefunctions for 4.6 μm emitting preliminary-design STA-type QCL, at threshold, calculated with MOCVD−growth IFR parameters [4]. States 4 and g_4 are the *ul* level and a parasitic state, respectively.

MOCVD-grown wafers, with a nominal injector sheet-doping density, n_s, of 1.04×10^{11} cm^{-2}, were processed into 20 μm-wide, high-reflectivity (HR)-coated back facets, and 3 mm-long ridge-guide devices. As pointed out in Ref. [1], the devices provided the following electro-optical characteristics: J_{th} = 1.25 kA/cm^2; slope efficiency, η_{sl} = 4.65 W/A; R_{diff} = 1.3 Ω; and front-facet maximum wall-plug efficiency, $\eta_{wp,max}$ = 17.8%. PICT action was achieved since the R_{diff} value (i.e., 1.3 Ω) was significantly smaller that the value for conventional QCLs of same pumped area (2.33 Ω), and the maximum current density, J_{max}, had a high value of 5.9 kA/cm^2. Good fits to experimental values [1] were obtained for a waveguide loss, α_w, of 1.56 cm^{-1}, a rather high value, justified by the fact that the high J_{max} value indicated inadvertent injector overdoping. Indeed, in order to obtain that J_{max} value, an n_s value of 1.3×10^{11} cm^{-2} had to be used in modeling. Nevertheless, the excellent agreement found between experiment and theory [1] confirmed the accuracy of both the graded-interfaces model and the IFR parameters' values obtained from the analysis of APT results.

The $\eta_{wp,max}$ value (i.e., 17.8%) was lower than for GSMBE-grown 4.9 μm emitting ridge-guide QCLs with PICT action [2] (i.e., 25%). To realize why that happened, one has to look at the $\eta_{wp,max}$ expression [25]:

$$\eta_{wp,max} \cong \left(1 - \frac{J_{leak}}{J_{th}}\right) \eta_{tr} \frac{\alpha_m}{\alpha_m + \alpha_w} \left(1 - \frac{J_{th}}{J_{wpm}}\right) \frac{N_p h\nu}{q V_{wpm}} \quad (3)$$

where η_{tr} is the lasing-transition efficiency, J_{wpm} is the current density at the $\eta_{wp,max}$ point, N_p is the number of periods, hν is the photon energy, and V_{wpm} is the voltage at J_{wpm}. Part of the reason is that significant carrier leakage occurs for this preliminary design, as shown

below in Figure 7. The overall J_{leak}/J_{th} value is 23%, with leakage from the parasitic state g_4 through high-energy states 5 and 6, amounting to 11.5% (i.e., half the total leakage). Since J_{leak}/J_{th} for the 4.9 μm emitting ridge-guide QCL is [1] ~25%, the 1-J_{leak}/J_{th} term value is similar for both devices, as a result of the large parasitic-state leakage for this design. Then, given that the J_{th}/J_{wpm} values are basically the same (i.e., ~0.3), the main reason behind the lower $\eta_{wp,max}$ value is the higher α_w value (i.e., 1.56 cm^{-1} vs. 0.75 cm^{-1} for the 4.9 μm emitting ridge-guide QCL [25]). Indeed, the ratio of the quantities $\alpha_m/(\alpha_m + \alpha_w)$ for the two devices is 1.27, accounting for most of the 1.4 ratio of the $\eta_{wp,max}$ values. The rest of the difference comes from the ratio of the V_{wpm} values being ~ 1.1, primarily since the threshold voltage is ~10% higher (i.e., 13.3 V vs. 12 V).

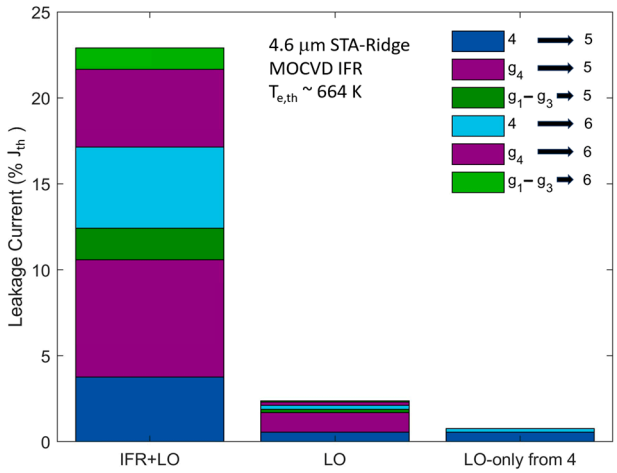

Figure 7. Bar graphs of the components of the normalized leakage-current density through the active-region energy states 5 and 6, for the preliminary-design 4.6 μm emitting STA-type QCL modeled with MOCVD-growth IFR parameters [4]. LO and LO-only from 4 stand for leakage triggered only by LO-phonon scattering in the presence of elastic scattering, and leakage from only the *ul* level, state 4, in the absence of elastic scattering, respectively. State g_4 is a parasitic state.

The grown QCL material was further processed into 5 mm long buried-heterostructure (BH) devices with HR-coated back facets and 10% reflectivity front-facet coatings, for 6 μm and 5 μm wide buried ridges. The electro-optical characteristics for a 6 μm wide BH-ridge device are shown in Figure 8a,b, together with the theoretically derived characteristics. The α_w value, from matching experimental data, was found to be 1.3 cm^{-1}, which makes sense, since it is smaller than the ridge-guide value by 0.26 cm^{-1}, a quantity typical of sidewall-scattering losses for ~20 μm wide ridge-guide QCLs [25]. A maximum front-facet, peak-pulsed wall-plug efficiency value of 19.1% is obtained. This value is higher than the best front-facet results reported to date, at room temperature, from vertical-transition (i.e., no PICT action) 4.6–5.0 μm emitting QCLs [26,27]: 15.1% and 14%, respectively. However, the result is lower than the record value (i.e., 27%) obtained from the 4.9 μm emitting BH QCL [2]. We attribute the difference to two issues: (a) the difference in α_w values (i.e., 1.3 cm^{-1} vs. 0.5 cm^{-1}), giving an $\alpha_m/(\alpha_m + \alpha_w)$ ratio of 1.29; and (b) the ratio of the V_{wpm} values is 1.08, since a higher R_{diff} value (2.35 Ω) reflects a pumped area 75% that of the 4.9 μm emitting BH QCL.

With further design optimizations, for low normalized leakage-current-density (i.e., ≤10%) designs and optimization of the crystal-growth conditions for lowering the α_w value, the maximum WPE value will significantly increase.

Under CW operating conditions, the 6 μm wide BH-ridge devices provided 2.3 maximum CW power and 13.7% maximum CW wall-plug efficiency. However, the CW L-I curve displayed kinks, indicating the excitation of high-order spatial modes.

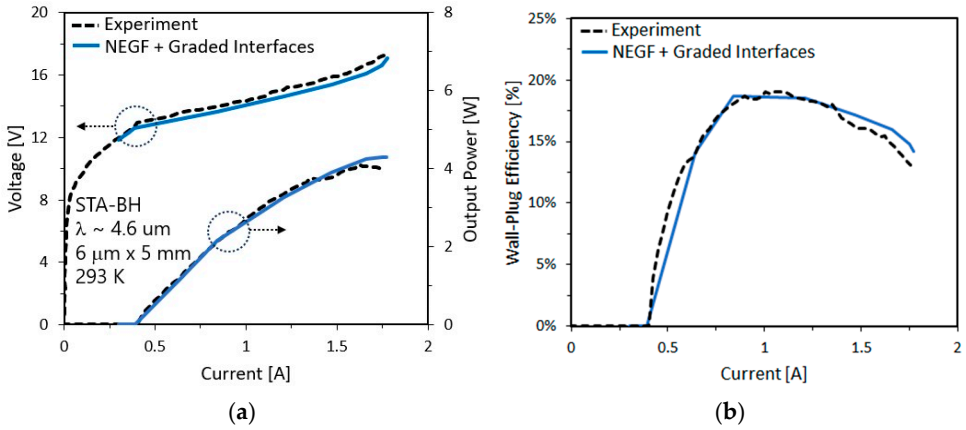

(**a**) (**b**)

Figure 8. BH-type, HR/LR-coated laser fabricated from STA-QCL material of preliminary PICT-action design: (**a**) the L-I-V and (**b**) the WPE-I curves. The solid curves are calculated curves.

For 5 μm wide buried-ridge chips, we obtained pure diffraction-limited beams (M^2 (x) = 1.06 and M^2 (y) = 1.05) (Figure 9b), where *x* is the lateral direction, to 1.3 W quasi-CW (100 μs pulse, 2% duty cycle) output power; thus, at the same drive current value the device reached 1.3 W CW (Figure 9a). That is, the device operated in a single spatial mode to the maximum CW power.

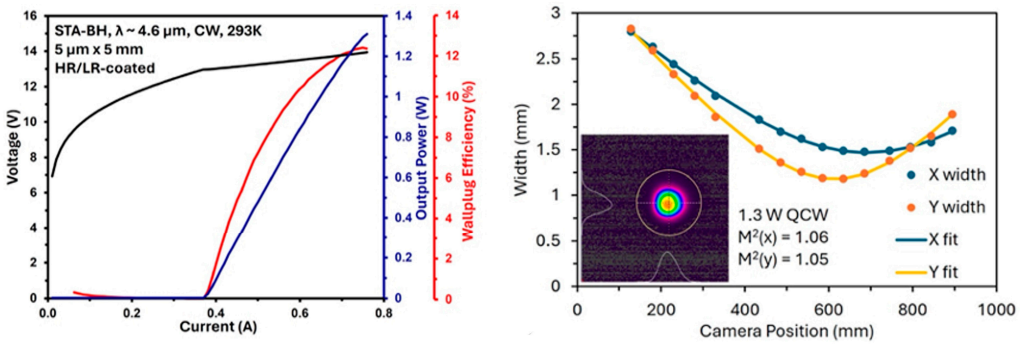

(**a**) (**b**)

Figure 9. The 5 μm × 5 mm BH-type STA-QCL: (**a**) CW L-I-V curves; and (**b**) beam width vs. position data and fitted curves used for calculating the beam quality factor, M^2, in the lateral and transverse directions, and an example beam profile 457 mm away from focus (inset).

We measured the beam quality factor, M^2, following the procedure in ISO 11146-1:2005(E) (ANSI), where beam width versus position data taken after a focusing lens is fit to a parabola, and the fitting parameters are used to compute M^2 for each axis. The 5 μm × 5 mm QCL was first collimated using a high-NA 0.8 mm focal length lens and then focused using a parabolic mirror with 500 mm focal length. The beam size at the 4-sigma points is measured on both axes at ~5 cm intervals as the camera is moved along the beam path after the focusing mirror. Figure 9b shows the resulting data and an example beam profile used for calculating the beam width. At the bias point corresponding to 1.3 W peak QCW output power, we measured M^2 values of 1.06 for the *x*-axis and 1.05 for the *y*-axis.

4.2. Low-Leakage 4.7 μm Emitting STA-QCLs with PICT Action

4.2.1. Considering Current MOCVD-Growth IFR Parameters

An optimized design, considering our current MOCVD-growth IFR parameters mentioned above, was performed for eliminating parasitic states and increasing the E_{54} and $E_{5,g3}$ values. The device considered is a BH device, which, for comparison purposes, has the

same buried-ridge dimensions, sheet-doping density, mirror loss, and heatsink temperature as the 4.9 μm emitting record-WPE QCL [2]: 8 μm × 5 mm, 0.9×10^{11} cm^{-2}, 2.26 cm^{-1}, and 298 K, respectively. The waveguide loss is calculated as follows [18]:

$$\alpha_w = \alpha_{empty} + \Gamma\alpha_{nr} \quad (4)$$

where α_{empty} is the empty-cavity loss; Γ is the optical confinement factor to the core region; and α_{nr} is the core-material, nonresonant intersubband-loss coefficient, which is dependent on the interfacial quality of the grown material [26]. For α_{empty} we take the same value we calculated for the 4.9 μm emitting record-WPE QCL: 0.16 cm^{-1}. From the experimental fits to ridge-guide devices [1] and BH devices (Figure 8), α_{nr} is found to be 1.7 cm^{-1} when n_s is 1.3×10^{11} cm^{-2}. Since α_{nr} is proportional [28] with n_s, for a 0.9×10^{11} cm^{-2} n_s value, the corresponding α_{nr} value is 1.2 cm^{-1}. Then, using Γ = 0.67, the α_w value is 0.96 cm^{-1}. The deduced α_{nr} value is consistent with the 1.05 cm^{-1} value we obtained from an analysis of 7.8 μm emitting ridge-guide QCLs [29] of the same n_s value, thus confirming the accuracy of its derivation.

The conduction-band diagram and relevant wavefunctions are shown in Figure 10. In the optical-transition region, there are two moderate-height barriers ($Al_{0.54}In_{0.46}As$ and $Al_{0.70}In_{0.30}As$), followed by a tall, 1.2 nm thick barrier (AlAs), with corresponding Δ values of 0.14 nm and 0.2 nm. The *ul* level is state 4, at threshold, just as found above for the 8.3 μm emitting QCL (Figure 1a), except that the prior-stage, low-energy state 2′ corresponds to state g_3, while the next-higher-energy state, state 2″, corresponds to state 4. There is a strong diagonal transition (i.e., $z_{ul,ll}$ = 9.6 Å).

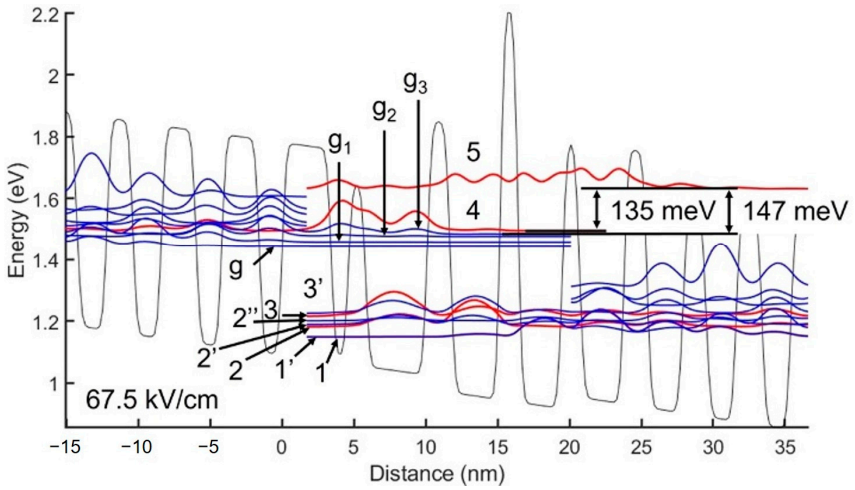

Figure 10. Conduction-band diagram and relevant wavefunctions for the low-leakage, 4.7 μm emitting design STA-QCL, at threshold, calculated with MOCVD-growth IFR parameters [4]. State 4 is the upper laser level.

The carrier-leakage bar chart is shown in Figure 11. Leakage occurs mostly from the *ul* level, state 4, and somewhat from state g_3. There is a more significant leakage from the *ul* level than from state g_3, since the *ul* level is hotter than that level (i.e., 654 K vs. 590 K); is closer to state 5 than that level (135 meV vs. 147 meV); and has a higher IOF value, at interfaces with state 5, than that level (1.63×10^{-4} vs. 1.08×10^{-4}). The overall J_{leak}/J_{th} value is moderately low: 17.5%.

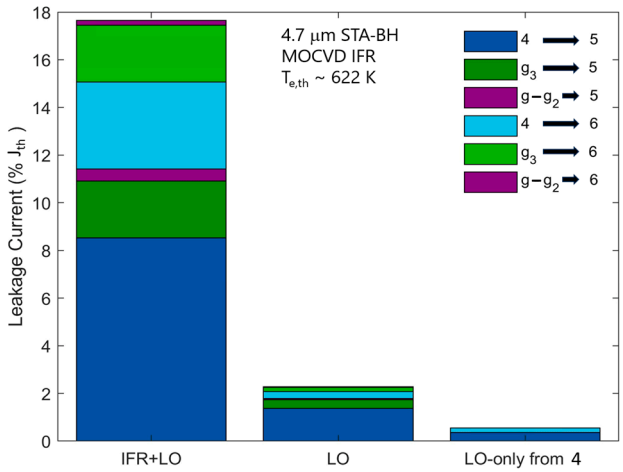

Figure 11. Bar graphs of the components of the normalized leakage-current density through the active-region energy states 5 and 6 for the low-leakage, 4.7 μm emitting STA-QCL design modeled with MOCVD-growth IFR parameters. LO and LO-only from 4 stand for leakage triggered only by LO-phonon scattering in the presence of elastic scattering, and leakage from the *ul* level, state 4, in the absence of elastic scattering, respectively.

The calculated L-I-V and WPE-I curves are shown in Figure 12a,b. The R_{diff} and J_{max} values are 1.8 Ω and 4.4 kA/cm^2, respectively, indicating PICT action. However, the J_{max} value is significantly lower than that for the 4.9 μm emitting record-WPE QCL [2]: 5.7 kA/cm^2. The reason for this difference is due to two factors: (a) the dipole matrix element is larger than for the 4.9 μm emitting QCL, i.e., 9.6 Å vs. 6.7 Å, thus leading to less lasing-transition diagonality and, in turn, weaker PICT action [1]; and (b) injection at threshold into the *ul* level occurs from state g_3, as opposed to from a higher energy state, state g_4, for the 4.9 μm emitting QCL [1]. Thus, since for both devices J_{max} occurs at the resonance between the *ul* level and a low-energy state, state g_1, there is a smaller dynamic range in field strength, from lasing threshold to J_{max}, for this device than for the 4.9 μm emitting QCL: 11.5 kV/cm vs. 18.3 kV/cm, resulting in a lower J_{max} value.

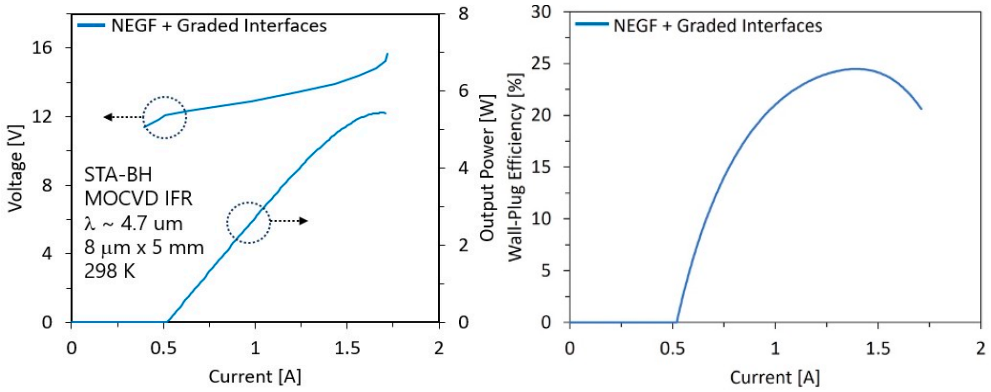

Figure 12. Low-leakage, 4.7 μm emitting STA-QCL design modeled with MOCVD-growth IFR parameters: (**a**) L-I-V curves, and (**b**) WPE-I curve.

The threshold-current density, J_{th}, is 1.32 kA/cm^2, virtually the same as for the GSMBE-grown 4.9 μm emitting record-WPE QCL [2]. The slope efficiency, η_{sl}, value is 5.69 W/A, which is similar to the 5.72 W/A value for the 4.9 μm emitting QCL [2]. The reason the η_{sl} values are similar is that the lower α_w value for the GSMBE-grown vs. MOCVD-grown devices (i.e., 0.5 cm^{-1} vs. 0.96 cm^{-1}) is basically compensated for by significantly lower

normalized carrier leakage (17.5% vs. 28%). The $\eta_{wp,max}$ value is 24.5%, that is, somewhat lower than the one for 4.9 μm emitting QCL (27%). (The difference is due to the ratio of the 1-J_{th}/J_{wpm} values: 1.1.) Thus, with our current MOCVD-grown material, similarly high $\eta_{wp,max}$ values can be obtained as for the 4.9 μm emitting record-WPE QCL [2], since the higher α_w value is compensated for by carrier-leakage suppression.

4.2.2. Considering the IFR Parameters of Optimized-MBE-Growth Interfaces

Now, by using the graded-interface IFR parameters obtained in Ref. [1] for the 4.9 μm emitting record-WPE QCL and the measured [2] α_w value of 0.5 cm^{-1}, corresponding to an α_{nr} value of 0.5 cm^{-1}, we calculate the characteristics for the low-leakage, 4.7 μm emitting QCL design. Figure 13 shows the conduction-band diagram and relevant wavefunctions. The two moderate-height barriers and the tall barrier are the same as for the MOCVD-growth case, except that the employed Δ values are 0.10 nm, 0.13 nm, and 0.17 nm, and L is 0.4 nm, just as for the 4.9 μm emitting QCL [1]. In this case, as mentioned above, since the injecting state, state g_3, has significantly higher differential gain than state 4, state g_3 is the *ul* level, from threshold (see Figure 1b) to the g_3-4 resonance at 1.8 × threshold. The F_{th} value is lower than for the MOCVD-growth device (i.e., 65 kV/cm vs. 67.5 kV/cm). The E_{54} and $E_{5,g3}$ values have increased to 154 meV and 142 meV, respectively, as expected for a lower F_{th} value. This is in part responsible for a lower normalized leakage-current density. The IOF values, at interfaces with state 5, for the *ul* level and state 4 are 0.64 × 10^{-4} and 2.1 × 10^{-4}, respectively, vs. 1.69 × 10^{-4} and 1.81 × 10^{-4} for the linear-taper active-region design of the 4.9 μm emitting record-WPE QCL [2]. That is, as shown in Ref. [5], the linear barrier-height tapering for the 4.9 μm emitting QCL leads to a high IOF value between the *ul* level and the next-higher-energy level, state 5. The diagonal transition is much stronger (i.e., the $z_{ul,ll}$ = 6.2 Å) than for the MOCVD-growth STA-type device.

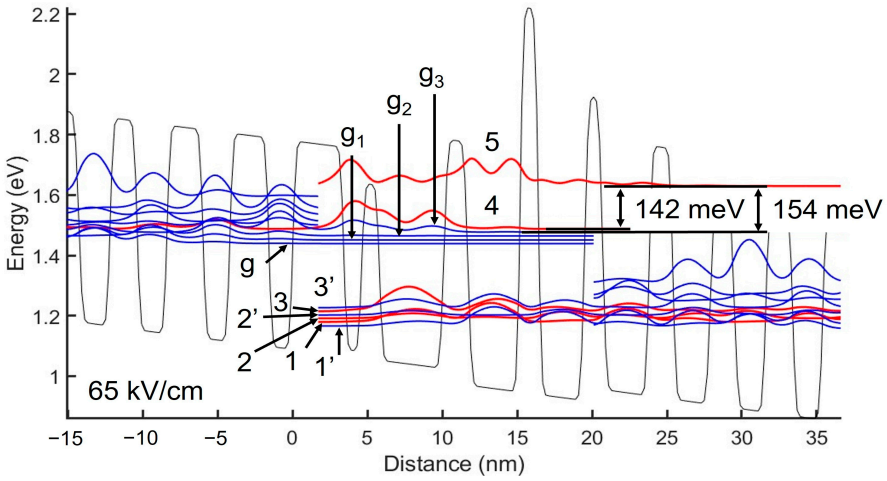

Figure 13. Conduction band diagram and relevant wavefunctions for the low-leakage, 4.7 μm emitting STA-QCL design, at threshold, calculated with optimized-MBE-growth IFR parameters [1]. State g_3 is the upper laser level.

The carrier-leakage bar chart is shown in Figure 14. There is much more leakage from state 4 than from *ul* level, since state 4 is hotter than the *ul* level (i.e., 622 K vs. 548 K) and closer to state 5 than the *ul* level (142 meV vs. 154 meV). As a result of higher E_{54} and $E_{5,g3}$ values and somewhat lower electron temperatures than for the MOCVD-growth case, the overall J_{leak}/J_{th} value is quite low: 13.5%.

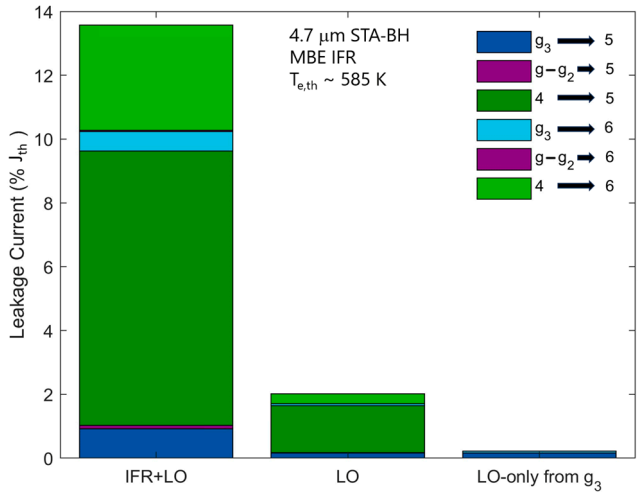

Figure 14. Bar graphs of the components of the normalized leakage-current density through the active-region energy states 5 and 6 for the low-leakage, 4.7 μm emitting STA-type QCL modeled with optimized-MBE-growth IFR parameters. LO and LO-only from g_3 stand for leakage triggered only by LO-phonon scattering in the presence of elastic scattering, and leakage only from the *ul* level, state g_3, in the absence of elastic scattering, respectively.

For a simple comparison to the carrier leakage in the 4.9 μm emitting record-WPE QCL [1], we compare leakages only through state 5 (i.e., 9.5% vs. 17%). Leakages from the *ul* level through state 5 are significantly different: 0.75% vs. 5%. This reflects both a higher $E_{5,ul}$ value (i.e., 154 meV vs. 120 meV) and an IOF value 2.6 times smaller than for the 4.9 μm emitting QCL. As for leakages from state 4 to state 5, 8.5% vs. 11.5%, the difference primarily reflects the higher E_{54} value (i.e., 142 meV vs. 112.5 meV). Thus, the STA design approach severely suppresses leakage from the *ul* level through state 5, and it suppresses leakage from state 4 through state 5. The leakage through state 6 decreases from 11% to 4%. The net effect is basically halving the normalized leakage-current density compared to that for the linear-taper active-region design employed for the 4.9 μm emitting QCL [2] (i.e., 13.5% vs. 28%).

The L-I-V and WPE-I curves are shown in Figure 15a,b. The R_{diff} and J_{max} values are 1.47 Ω and 4.9 kA/cm^2, respectively, indicating stronger PICT action than for the case with MOCVD-growth IFR parameters. This proves that, indeed, when a prior-stage, low-energy state is the *ul* level, at threshold, the PICT action is stronger. The J_{th} value is 1.32 kA/cm^2, basically the same as for the 4.9 μm emitting record-WPE QCL [2]. However, the η_{sl} value is 7 W/A, which is significantly higher than the 5.72 W/A value for the 4.9 μm emitting QCL [2]. The 22% higher η_{sl} value is primarily due to the 20% increase in the $1 - J_{leak}/J_{th}$ term value. Because the η_{tr} value is found to be basically the same, i.e., 97%, the internal differential efficiency [6], $\eta_i \cong (1 - J_{leak}/J_{th})\eta_{tr}$, reaches a value of 83%, which is significantly higher than the 70% value obtained for the 4.9 μm emitting QCLs [2].

Notably, although there is stronger PICT action than for the 4.9 μm emitting QCL (i.e., a R_{diff} value of 1.47 Ω vs. 1.7 Ω) due to a stronger diagonal transition (i.e., the $z_{ul,ll}$ value is 6.2 Å vs. 6.7 Å), the J_{max} value is somewhat smaller than that for 4.9 μm emitting QCL (i.e., 4.9 kA/cm^2 vs. 5.7 kA/cm^2). The latter is a consequence of injection into the *ul* level happening at threshold from state g_3 rather than from the higher energy state, state g_4, for the 4.9 μm emitting QCL [1]. That is, the dynamic range in applied-field strength, from threshold to J_{max}, is 16.9 kV/cm vs. 18.3 kV/cm for the 4.9 μm emitting QCL, which explains the higher J_{max} value. Notwithstanding, the significantly higher slope efficiency, due to substantial carrier-leakage suppression, results in basically the same maximum power value: 7.7 W vs. 8.3 W [2].

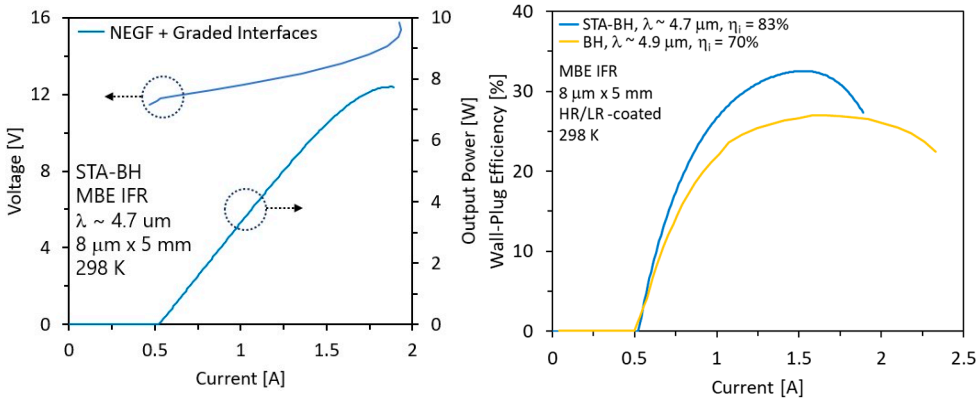

(**a**) (**b**)

Figure 15. Low-leakage, 4.7 μm emitting STA-QCL design modeled with optimized-MBE-growth IFR parameters: (**a**) L-I-V curves; and (**b**) WPE-I curves including, for comparison, that for the 4.9 μm emitting QCL [2]. Reproduced from [2] with the permission of AIP Publishing.

The $\eta_{wp,max}$ value is 33%, so it is a front-facet value that is significantly higher than the record value reported for the 4.9 μm mitting QCL [2] (i.e., 27%). The values for the terms $(1 - J_{th}/J_{wpm})$ and $h\nu/V_{wpm}$ in Equation (3) cancel each other out; thus, the relative increase in the $\eta_{wp,max}$ value (i.e., 22%) reflects the 22% increase in the η_{sl} value. In the limit of no leakage, with the terms $1 - J_{leak}/J_{th}$ and $1 - J_{th}/J_{wpm}$ modified accordingly, and assuming that the V_{wpm} value stays basically the same for small variations in J_{leak}/J_{th}, which can be seen to be correct from the V-I plots above for the MOVCD-growth and MBE-growth devices (i.e., 13.4 V), the ultimate $\eta_{wp,max}$ value is estimated to be 40.1%. We ran the graded-interfaces NEGF model with cancelled carrier leakage by lowering the allowed energy value so as to delete the high-energy states 5 and 6. Then, the maximum $\eta_{wp,max}$ value is found to be 41.8%, slightly above our estimate, and interestingly, in good agreement with a prior estimate of ~41%, at λ = 4.7 μm, for abrupt-interfaces QCLs [6]. We conclude that, for 4.7 μm emitting QCLs, the ultimate $\eta_{wp,max}$ value is ~41%.

5. Conclusions

Graded-interfaces modeling has allowed for the uncovering of unique features of high-performance mid-IR QCLs. First and foremost, injection into the *ul* level primarily occurs from prior-stage energy states via sequential resonant tunneling in the presence of scattering over wide multiple-barrier regions. This enables the quick gain recovery required for devices with strong photon-induced carrier transport (PICT), the key design feature for record-high WPE operation.

A notable exception is a device for which, at threshold, the differential gain is higher for the transition involving the injecting state than for the transition involving the injected-in state, in which case the injecting state is the *ul* level up to its resonance with the injected-in state. Then, over that drive range, the device is an injectionless QCL, which leads to even quicker gain recovery for PICT-action devices, since the only time delay is thermalization from the *ll* level to the next-stage *ul* level. This, in turn, leads to even stronger PICT action, which explains why QCLs of the highest reported or projected WPE values are, at and close above threshold, injectionless devices.

By using graded-interfaces modeling coupled with the carrier-leakage suppression of the STA design, we obtain, from a preliminary-design 4.6 μm emitting QCL, 19.1% front-facet WPE, the highest WPE reported to date from MOCVD-grown QCLs. A low-leakage, 4.7 μm emitting STA design, employing MOCVD-growth IFR parameters and waveguide loss, α_w, provides 24.5% front-facet WPE, a value comparable to the record-

WPE value reported from optimized-MBE-growth QCLs, since carrier-leakage suppression compensates for a higher α_w value. Finally, the low-leakage design with optimized-MBE-growth IFR parameters and α_w values provides a 33% front-facet WPE, a value higher than the current WPE record, approaching the ~41% fundamental limit at λ = 4.7 μm.

Recently, by optimizing their MOCVD crystal-growth conditions, Fei et al. [10] have reported a measured α_w value of 0.66 cm^{-1}, at similar sheet-doping density (i.e., 0.95×10^{11} cm^{-2}) and number of stages (40) as for the GSMBE-grown 4.9 μm emitting QCL [2], for a 4.6 μm emitting conventional-design (i.e., no PICT action) QCL. That is, with optimized MOCVD-growth conditions, α_w values quite close to the lowest value reported from optimized-interfaces GSMBE-grown devices (i.e., 0.5 cm^{-1}) can be obtained. Furthermore, by iteratively improving the graded-interfaces quality by optimizing the MOCVD crystal-growth conditions in conjunction with APT analysis, in order to lower the α_{nr} value, α_w values as low as 0.6 cm^{-1} should be achievable. Then, by taking α_w = 0.6 cm^{-1}, the projected maximum WPE value at λ = 4.7 μm becomes 32%. From our experience with graded-interfaces modeling of STA-type QCLs, we believe that the normalized leakage-current density can be further lowered to the 8–10% range, thus allowing that MOCVD-grown QCLs can also achieve maximum WPE values approaching the ~ 41% fundamental limit.

Graded-interfaces modeling is suitable for characterizing and designing most QCL structures grown by MOCVD or MBE. A notable exception appears to be devices that have atomic-species segregation, which causes relatively large, asymmetric graded-interfaces widths for structures grown in specific reactors by either MOCVD or MBE [8,12]. Then, for graded-interfaces modeling the design method used in [8,11] (i.e., employing measured QCL electroluminescence wavelengths for deducing an empirical, symmetric graded-interface width) is suitable only for obtaining the desired lasing wavelength. To date, only superlattices grown without atomic-species segregation [4,12] have been successfully used for measuring via APT all graded-interface IFR parameters, including relatively small and symmetric graded-interface widths. Measuring all IFR parameters is critical to designing devices of performances approaching fundamental limits, since the carrier leakage that needs to be suppressed is dominated by IFR scattering [1].

While graded-interfaces modeling is clearly the design tool for high-power, high-efficiency mid-IR QCLs, it also appears to hold great potential as the design approach for realizing THz QCLs operating at room temperature (RT). The THz devices that hold the current record for maximum operating temperature, T_{max} [30], are tall-barrier, two-well (TW) QCLs for which LO-phonon thermally activated carrier leakage has been substantially suppressed. However, a recent NEGF-based study by Gower et al. [31] found that for nearly identical, abrupt-interfaces TW designs grown in two different MBE reactors, although the NEGF modeling approach predicts a similarly high T_{max} value (~250 K), the experimental T_{max} values were significantly different. Gower et al. further found that this discrepancy can be justified by assuming different abrupt-interfaces Δ values, and that their finding may in fact reflect different IFR-triggered, thermally activated carrier-leakage values at graded interfaces. That is, with the significant increase in barrier height for TW devices, the impact of graded interfaces on THz-QCL performance should not be neglected. This is true especially since graded interfaces are likely to cause the wavefunctions of high-energy active-region states to have high overlap-at-interfaces values with the *ul* level and other states' wavefunctions, thus leading to shunt-type, IFR-triggered carrier leakage, just like in mid-IR QCLs. Then, suppressing such carrier leakage by improving the interface quality through iterative changes in crystal-growth conditions, while concurrently using for redesign graded-interface IFR parameters obtained via APT, may well allow for the long-sought goal of RT operation to be achieved.

Author Contributions: Conceptualization, D.B., S.S. and T.G.; software, S.S. and T.G.; formal analysis, D.B., S.S. and R.A.M.; investigation, D.B., H.G. and R.A.M.; data curation, S.S.; writing—original draft preparation, D.B. and S.S.; writing—review and editing, T.G., L.J.M. and R.A.M.; visualization, S.S., H.G. and J.D.K.; supervision, D.B., L.J.M. and R.A.M.; project administration, D.B. and R.A.M.; funding acquisition, D.B. and R.A.M. All authors have read and agreed to the published version of the manuscript.

Funding: This research was funded by the U.S. NAVY, grants N68335-19-C-0196 (J. Sugrim) and N68936-23-C-0002 (R. LaMarca). The research at University of Wisconsin–Madison reported in this paper was supported via funding provided by Intraband, LLC, with which D. Botez and L. J. Mawst have significant financial interest.

Institutional Review Board Statement: Not applicable.

Informed Consent Statement: Not applicable.

Data Availability Statement: The datasets generated and/or analyzed during the current study are available from the corresponding author upon reasonable request.

Acknowledgments: The authors gratefully acknowledge valuable discussions with Sushil Kumar.

Conflicts of Interest: Robert A. Marsland is employed by Intraband LLC. The authors declare that they have no known competing financial interests or personal relationships that could have appeared to influence the work reported in this paper.

References

1. Suri, S.; Knipfer, B.B.; Grange, T.; Gao, H.; Kirch, J.D.; Mawst, L.J.; Marsland, R.A.; Botez, D. Modeling with graded interfaces: Tool for understanding and designing record-high power and efficiency mid-infrared quantum cascade lasers. *Nanophotonics* **2024**, *13*, 1745–1757, Erratum in *Nanophotonics* **2024**, *13*, 4849. [CrossRef]
2. Bai, Y.; Bandyopadhyay, N.; Tsao, S.; Slivken, S.; Razeghi, M. Room temperature quantum cascade lasers with 27% wall plug efficiency. *Appl. Phys. Lett.* **2011**, *98*, 181102. [CrossRef]
3. Zhou, W.; Lu, Q.-Y.; Wu, D.-H.; Slivken, S.; Razeghi, M. High-power, continuous-wave, phase-locked quantum cascade laser arrays emitting at 8 μm. *Opt. Express* **2019**, *27*, 15776–15785. [CrossRef]
4. Knipfer, B.; Xu, S.; Kirch, J.D.; Botez, D.; Mawst, L.J. Analysis of interface roughness in strained InGaAs/AlInAs quantum cascade laser structures (λ∼4.6 μm) by atom probe tomography. *J. Cryst. Growth* **2022**, *583*, 126531. [CrossRef]
5. Boyle, C.; Oresick, K.M.; Kirch, J.D.; Flores, Y.V.; Mawst, L.J.; Botez, D. Carrier leakage via interface-roughness scattering bridges gap between theoretical and experimental internal efficiencies of quantum cascade lasers. *Appl. Phys. Lett.* **2020**, *117*, 051101, Erratum: *Appl. Phys. Lett.* **2020**, *117*, 109901. [CrossRef]
6. Botez, D.; Mawst, L.J. State-of-the-Art Mid-Infrared QCLs: Elastic Scattering, High CW Power and Coherent-Power Scaling. In *Mid-Infrared and Terahertz Quantum Cascade Lasers*; Botez, D., Belkin, M.A., Eds.; Cambridge University Press: Cambridge, UK, 2023; pp. 41–101.
7. Botez, D.; Shin, J.C.; Kirch, J.D.; Chang, C.-C.; Mawst, L.J.; Earles, T. Multidimensional conduction-band engineering for maximizing the continuous-wave (CW) wall-plug efficiencies of mid-infrared quantum cascade lasers. *IEEE J. Sel. Top. Quantum Electron.* **2013**, *19*, 1200312, Correction: *IEEE J. Sel. Top. Quantum Electron.* **2013**, *19*, 9700101. [CrossRef]
8. Wang, C.A.; Schwarz, B.; Siriani, D.F.; Missaggia, L.J.; Connors, M.K.; Mansuripur, T.S.; Calawa, D.R.; McNulty, D.; Nickerson, M.; Donnelly, J.P.; et al. MOVPE growth of LWIR AlInAs/GaInAs/InP quantum cascade lasers: Impact of growth and material quality on laser performance. *IEEE J. Sel. Top. Quantum Electron.* **2017**, *23*, 1200413. [CrossRef]
9. Bugajski, M.; Kolek, A.; Hałdas, G.; Strupinski, W.; Pasternak, I.; Kołkowski, W.; Pierscinski, K. MOCVD grown InGaAs/InAlAs quantum cascade lasers emitting at 7.7 μm. *Photonics* **2024**, *11*, 1195. [CrossRef]
10. Fei, T.; Zhai, S.; Zhang, J.; Lu, Q.; Zhuo, N.; Liu, J.; Wang, L.; Liu, S.; Jia, Z.; Li, K.; et al. 3 W continuous-wave room temperature quantum cascade laser grown by metal-organic chemical vapor deposition. *Photonics* **2023**, *10*, 47. [CrossRef]
11. Wang, C.; Schwarz, B.; Siriani, D.; Connors, M.; Missaggia, L.; Calawa, D.; McNulty, D.; Akey, A.; Zheng, M.; Donnelly, J.; et al. Sensitivity of heterointerfaces on emission wavelength of quantum cascade lasers. *J. Cryst. Growth* **2017**, *464*, 215–220. [CrossRef]
12. Grange, T.; Mukherjee, S.; Capellini, G.; Montanar, M.; Persichetti, L.; Di Gaspare, L.; Birner, S.; Attiaoui, A.; Moutanabbir, O.; Virgilio, M.; et al. Atomic-scale insights into semiconductor heterostructures: From experimental three-dimensional analysis of the interface to a generalized theory of interfacial roughness scattering. *Phys. Rev. Appl.* **2020**, *13*, 044062. [CrossRef]

13. Schwarz, B.; Wang, C.A.; Missaggia, L.J.; Mansuripur, T.S.; Chevalier, P.; Connors, M.K.; McNulty, D.; Cederberg, J.; Strasser, G.; Capasso, F. Watt-level continuous-wave emission from a bifunctional quantum cascade laser/detector. *ACS Photonics* **2017**, *4*, 1225–1231. [CrossRef]
14. Blaser, S.; Diehl, L.; Beck, M.; Faist, J.; Oesterle, U.; Xu, J.; Barbieri, S.; Beltram, F. Characterization and modeling of quantum cascade lasers based on a photon-assisted tunneling transition. *IEEE J. Quantum Electron.* **2001**, *37*, 448–455. [CrossRef]
15. Choi, H.; Diehl, L.; Wu, Z.-K.; Giovannini, M.; Faist, J.; Capasso, F.; Norris, T.B. Time-resolved investigations of electronic transport dynamics in quantum cascade lasers based on diagonal lasing transition. *IEEE J. Quantum Electron.* **2009**, *45*, 307–319. [CrossRef]
16. Khurgin, J.B.; Dikmelik, Y.; Liu, P.Q.; Hoffman, A.J.; Escarra, M.D.; Franz, K.J.; Gmachl, C.F. Role of interface roughness in the transport and lasing characteristics of quantum cascade lasers. *Appl. Phys. Lett.* **2009**, *94*, 091101. [CrossRef]
17. Sirtori, C.; Capasso, F.; Faist, J.; Hutchinson, A.L.; Sivco, D.L.; Cho, A.Y. Resonant tunneling in quantum cascade lasers. *IEEE J. Quantum Electron.* **1998**, *34*, 1722–1729. [CrossRef]
18. Faist, J. *Quantum Cascade Lasers*; Oxford University Press: Oxford, UK, 2013.
19. Soleimanikahnoj, S.; King, M.L.; Knezevic, I. Density-matrix model for photon-driven transport in quantum cascade lasers. *Phys. Rev. Appl.* **2021**, *15*, 034045. [CrossRef]
20. Matyas, A.; Lugli, P.; Jirauschek, C. Photon-induced carrier transport in high-efficiency mid-infrared quantum cascade lasers. *J. Appl. Phys.* **2011**, *110*, 013108. [CrossRef]
21. Lindskog, M.; Wolf, J.M.; Trinite, V.; Liverini, V.; Faist, J.; Maisons, G.; Carras, M.; Aidam, R.; Ostendorf, R.; Wacker, A. Comparative analysis of quantum cascade laser modeling based on density matrices and non-equilibrium Green's functions. *Appl. Phys. Lett.* **2014**, *105*, 103106. [CrossRef]
22. Bismuto, A.; Terazzi, R.; Beck, M.; Faist, J. Electrically tunable, high-performance quantum cascade laser. *Appl. Phys. Lett.* **2010**, *96*, 141105. [CrossRef]
23. Bai, Y.; Slivken, S.; Kuboya, S.; Darvish, S.R.; Razeghi, M. Quantum cascade lasers that emit more light than heat. *Nat. Photonics* **2010**, *4*, 99–102.
24. Faist, J.; Hofstetter, D.; Beck, M.; Aellen, T.; Rochat, M.; Blaser, S. Bound-to-continuum and two-phonon resonance quantum-cascade lasers for high duty cycle, high-temperature operation. *IEEE J. Quantum Electron.* **2002**, *38*, 533–546.
25. Botez, D.; Chang, C.-C.; Mawst, L.J. Temperature sensitivity of the electro-optical characteristics for mid-infrared (λ = 3–16 μm)-emitting quantum cascade lasers. *J. Phys. D: Appl. Phys.* **2016**, *49*, 043001. [CrossRef]
26. Lyakh, A.; Maulini, R.; Tsekoun, A.; Go, R.; Pflugl, C.; Diehl, L.; Wang, Q.J.; Capasso, F.; Patel, C.K.N. 3 W continuous wave room-temperature single-facet emission from quantum cascade lasers based on nonresonant extraction design approach. *Appl. Phys. Lett.* **2009**, *95*, 141113.
27. Botez, D.; Kirch, J.D.; Boyle, C.; Oresick, K.M.; Sigler, C.; Kim, H.; Knipfer, B.B.; Ryu, J.H.; Lindberg III, D.; Earles, T.; et al. High-efficiency, high-power mid-infrared quantum cascade lasers [Invited]. *Opt. Mater. Express* **2018**, *8*, 1378–1398, Erratum in *Opt. Mater. Express* **2021**, *11*, 1970. [CrossRef]
28. Khurgin, J.B. Basic Physics of Intersubband Radiative and Nonradiative Processes. In *Mid-Infrared and Terahertz Quantum Cascade Lasers*; Botez, D., Belkin, M.A., Eds.; Cambridge University Press: Cambridge, UK, 2023; pp. 5–40.
29. Oresick, K.M. Highly Efficient Long-Wavelength Infrared, Step-Taper Active-Region Quantum Cascade Lasers. Ph.D. Thesis, University of Wisconsin-Madison, Madison, WI, USA, April 2021.
30. Khalatpour, A.; Tam, M.C.; Addamane, S.J.; Reno, J.; Wasilewski, Z.; Hu, Q. Enhanced operating temperature in terahertz quantum cascade lasers based on direct phonon depopulation. *Appl. Phys. Lett.* **2023**, *122*, 161101.
31. Gower, N.L.; Levy, S.; Piperno, S.; Addamane, S.J.; Albo, A. Exploring the effects of molecular beam epitaxy growth characteristics on the temperature performance of state-of-the-art terahertz quantum cascade lasers. *Sci. Rep.* **2024**, *14*, 17411. [CrossRef] [PubMed]